8th GRACM International Congress on Computational Mechanics
Volos, 12 July – 15 July 2015

AN IMPLICIT 3D FINITE-VOLUME SCHEME FOR FREE-SURFACE FLOWS WITH SHOCKWAVES

Athanasios J. Klonidis and Johannes V. Soulis

Department of Civil Engineering
Fluid Mechanics / Hydraulics Division
Democritous University of Thrace
67100 Xanthi, Greece
e-mail: klonidis@gmail.com, soulis@civil.duth.gr.

Keywords: 3D finite-volume, implicit, boundary fitted coordinates, shockwaves, free-surface flow.

Abstract. *The proposed research work presents the development and application of an implicit finite-volume numerical scheme capable of simulating 3D, steady, free-surface flows in irregular geometry channels with shockwave presence. The Navier-Stokes equations are used together with the utilization of the pseudo-compressibility technique to calculate the pressure from the continuity equation. The position of the free surface is determined by applying a moving boundary condition through the inclusion of the two-dimensional depth-averaged mass continuity equation. All of the mentioned equations are transformed into non-orthogonal body-fitted coordinate system and approximated using a second order implicit scheme resulting from the linearization of the governing equations. To deal with significant numerical instabilities, resulting from dispersion errors appearing during the abrupt change of the free-surface position, an alternative numerical technique is presented leading to the utilization of two nested iteration steps. The resulting numerical model is used to simulate super-critical free-surface flows including discontinuous flow featured with shock waves. The comparisons are remarkably satisfactory.*

1 INTRODUCTION

For many years, in free-surface flow simulation problems it has been common to reduce the shallow water hydrodynamics to 2D. This practice has been proved to be valid when certain criteria are met. Yet, there are many cases where some or most of the 2D flow assumptions collapse. For example, in case the water flow meets a steep, curved bottom slope, an obstacle is interfered to the flow or an abrupt change occurs at the free-surface due to the presence of shock waves, velocity components will vary along all three dimensions and the pressure distribution will significantly diverge from the hydrostatic value. In such cases, the application of a 3D numerical model may provide more accurate results compared to a 2D one. One key difficulty arises when the Navier-Stokes equations are solved to simulate 3D free-surface flows. The position of the free-surface is not at priori known as it constitutes a moving boundary. Therefore, to answer the question "where exactly the free-surface is located" several numerical methods have been developed over the past years to tackle this task.

Pender and Manson[1] numerically solved the 3D incompressible Navier-Stokes equations combined with a k-ε turbulent model using a cell-centered finite volume scheme. In their model, the free-surface was treated as an ideal non-zero pressure rigid wall, defined as the highest level that the free-surface can potentially reach. This is known as the rigid lid technique. The well known SIMPLE algorithm (Semi-Implicit Method for Pressure-Linked Equations) was also modified to solve 3D free-surface flows by Ouillon and Dartus[2]. The basic feature of their proposed scheme lies upon the pressure-velocity decoupling technique. To determine the position of the free-surface, the porosity method was utilized according to which the model checks the rate of water each cell is filled with. The model was tested by simulating the flow field around a spur dike and numerical results were satisfactorily compared with available experimental data. Conclusion was also drawn from the simulation that wherever intense reversal flow occurs, non-hydrostatic pressure distribution becomes dominant. Feurich and Olsen [3] used a 3D numerical model to compute the free-surface for different cases of supercritical flows. Their model solved the Navier-Stokes equations on an unstructured hexahedral grid using the SIMPLE method and the k-ε turbulence model. The location of the free water surface was computed with the volume of fluid method.

In the present research work an alternative approach of three dimensional free surface flow simulations is investigated An implicit scheme was developed and properly adapted to track the free surface. The Navier-Stokes equations are coupled with the depth-averaged continuity equation. As a result, the free-surface is treated as a vertically moving boundary. No pressure-velocity decoupling or pressure-linked or any other additional

method is needed as the pressure value is calculated directly from the continuity equation, Chorin[4]. All equations are transformed into a non-orthogonal body-fitted coordinate system. To overcome the presence of dispersion errors due to rapid grid rearrangement, the model adopts an innovative procedure through which two nested iteration steps are used. All calculations take place within the inner iteration step but, as long as the iterations last, all values referring to the previous iteration remain unchanged. Upon convergence, the outer iteration step takes over to update the flow field. Also, the outer iteration step is responsible of controlling the final convergence. Following this procedure the model becomes highly stable and accurate. Another demonstrated feature of the model constitutes its ability to respond very well in both relatively coarse and fine grids. The latter is essential in computational time saving point of view. The model was used to analyze three-dimensional supercritical flows with the presence of shock waves. The computed results are tested against measurements as well as with two-dimensional numerical methods results.

2 MATHEMATICAL AND NUMERICAL FORMULATION

The flow is assumed to be homogenous, incompressible, three-dimensional, viscous with absence of Coriolis and wind forces. Chorin[4] proposed an alternative approach through which a factor β is introduced in the space derivatives of Navier-Stokes mass continuity equation while the density in the time derivative is substituted by the pressure. This procedure refers to as pseudo-compressibility technique. Thus, the under solution Navier-Stokes equations system becomes:

$$\begin{aligned} \frac{\partial P}{\partial t} + \frac{\partial (\beta \rho v_i)}{\partial x_i} &= 0 \\ \frac{\partial (\rho v_i)}{\partial t} + \frac{\partial (\rho v_j v_i)}{\partial x_j} &= -\frac{\partial P}{\partial x_j} + (f_i)_\tau + (f_i)_g \end{aligned} \tag{1}$$

The term $(f_i)_\tau$ represents the viscous stresses while the term $(f_i)_g = -\rho g \partial h / \partial x_i$ stands for the gravitational forces. In the present work the value of turbulent kinematic viscosity appearing in RHS of the system is determined with respect to the friction velocity u_* on the channel bottom as:

$$\begin{aligned} v_\tau &= \bar{v}_\tau = 0.1 h u_* \\ u_* &= \frac{\sqrt{\tau_{bx}^2 + \tau_{by}^2}}{\rho} \\ \tau_{bx} &= g h S_{fx}, \quad \tau_{by} = g h S_{fy} \end{aligned} \tag{2}$$

h is the vertical distance between free-surface and channel bottom and S_{fx}, S_{fy} are the bottom friction slopes along the x, y directions, respectively. Their values are determined with respect to Manning's roughness coefficient. The use of eqs (2) seems to be consistent with the developing type of flow in channels with smooth bed and walls discussed in the present work. Indeed, taking into account the work of Liu[5], in such flow types apart from the viscous sublayer where the flow is laminar, measurements showed that also in the turbulent logarithmic layer the turbulent shear stress is constant and equal to the bottom shear stress. Furthermore, by the modification of Prandtl's mixing length assumption, the logarithmic velocity profile applies also both to the transitional layer and the turbulent outer layer. Measured and computed velocities showed reasonable agreement. Therefore, from engineering point of view, even at high Reynolds numbers, a turbulent layer with the logarithmic velocity profile can be adequately assumed that covers the transitional layer, the turbulent logarithmic layer and the turbulent outer layer. With respect to the above, the model adopts a linear distribution of the bottom shear stress, τ_b, over the flow depth taking its higher value at the channel bottom and a zero value on the free-surface.

For the solution of eqs (1), regarding the free-surface flow problems, the following boundary conditions are applied:

- The pressure on the free-surface is zero.
- The fluid velocities v_x, v_y, v_z normal to bottom and solid boundaries are set equal to zero.
- During the fluid motion the fluid particles on the free-surface remain on it. Therefore, in the present study, the free-surface is treated as a moving boundary. Its vertical position h, calculated from the channel bottom,

is determined by introducing an additional partial differential equation; the depth-averaged continuity equation, Klonidis[6]:

$$\frac{\partial h}{\partial t}+\frac{\partial(h\bar{v}_x)}{\partial x}+\frac{\partial(h\bar{v}_y)}{\partial y}=0 \tag{3}$$

The main advantage of eqn (3) is that it includes the proper boundary conditions at the bottom and at the free surface. This approach brings a simple and robust method of finding the free surface location while automatically satisfying the mass conservation criterion. However, using this method some classes of free-surface flows like breaking and overturning waves, are excluded.

2.1 Transformation of flow equations

According to the proposed finite-volume scheme, hexahedra resulting from the construction of the physical domain are mapped onto cubes in the computational domain. This is accomplished through independent transformations from Cartesian *x, y, z* or global coordinates to local coordinate system ξ ,η ,ζ. Each cube in the computational domain comprises eight primary (hexahedra) elements of the physical domain. Detailed description of the transformation can be found, Klonidis[6]. Under the aforementioned transformation, eqn (1) takes the form:

$$\frac{\partial \hat{Q}}{\partial t}+\frac{\partial \hat{F}}{\partial \xi}+\frac{\partial \hat{G}}{\partial \eta}+\frac{\partial \hat{H}}{\partial \zeta}=\frac{\partial \hat{F}_v}{\partial \xi}+\frac{\partial \hat{G}_v}{\partial \eta}+\frac{\partial \hat{H}_v}{\partial \zeta}+\hat{W} \tag{4}$$

$$\hat{Q}=\begin{bmatrix} JP \\ J\rho v_x \\ J\rho v_y \\ J\rho v_z \end{bmatrix}, \hat{F}=\begin{bmatrix} J\beta\rho v_\xi \\ J(\rho v_x v_\xi + P\xi_x) \\ J(\rho v_y v_\xi + P\xi_y) \\ J(\rho v_z v_\xi + P\xi_z) \end{bmatrix}, \hat{G}=\begin{bmatrix} J\beta\rho v_\eta \\ J(\rho v_x v_\eta + P\eta_x) \\ J(\rho v_y v_\eta + P\eta_y) \\ J(\rho v_z v_\eta + P\eta_z) \end{bmatrix}, \hat{H}=\begin{bmatrix} J\beta\rho v_\zeta \\ J(\rho v_x v_\zeta + P\zeta_x) \\ J(\rho v_y v_\zeta + P\zeta_y) \\ J(\rho v_z v_\zeta + P\zeta_z) \end{bmatrix} \tag{5}$$

$$\overline{F}_v=\begin{bmatrix} 0 \\ J\bar{f}_{v2} \\ J\bar{f}_{v3} \\ J\bar{f}_{v4} \end{bmatrix}, \overline{G}_v=\begin{bmatrix} 0 \\ J\overline{g}_{v2} \\ J\overline{g}_{v3} \\ J\overline{g}_{v4} \end{bmatrix}, \overline{H}_v=\begin{bmatrix} 0 \\ J\bar{h}_{v2} \\ J\bar{h}_{v2} \\ J\bar{h}_{v2} \end{bmatrix}, \hat{W}=\begin{bmatrix} 0 \\ 0 \\ 0 \\ J\rho g \end{bmatrix} \tag{6}$$

where J is the Jacobian transformation matrix. In addition to the hydrodynamic equations, the depth-averaged continuity (global 2D) uation, eqn (3), also needs to be transformed into the local coordinate system. To solve this equation in the local coordinate system a new 2D computational grid is created. Thus, quadrilaterals in the physical domain are mapped onto squares in the computational domain, Klonidis and Soulis[7]. Each square in the computational domain comprises four primary (quadrilaterals) elements of the physical domain. Following the aforementioned procedure the transformed depth-averaged continuity equation takes the form:

$$\frac{\partial(Jh)}{\partial t}+\frac{\partial(Jh\bar{v}_\xi)}{\partial \xi}+\frac{\partial(Jh\bar{v}_\eta)}{\partial \eta}=0 \tag{7}$$

2.2 Numerical scheme

The numerical simulation of eqs (4) is achieved using a second-order accurate, implicit, finite-difference scheme. This scheme is produced following a procedure through which eqs (4) are linearized by expanding to Taylor series. Initially the time derivatives are linearized and thereafter the space derivatives. Forward differences are used for time derivatives and central differences for space derivatives. The above procedure yields:

$$\left(I+\frac{\Delta t}{2}\frac{\delta\hat{A}^n}{\Delta\xi}\right)\left(I+\frac{\Delta t}{2}\frac{\delta\hat{B}^n}{\Delta\eta}\right)\left(I+\frac{\Delta t}{2}\frac{\delta\hat{C}^n}{\Delta\zeta}\right)\Delta\hat{Q}^{n+1}= \\ -\frac{\Delta t}{2}\left(\frac{\delta\hat{F}^n}{\Delta\xi}+\frac{\delta\hat{G}^n}{\Delta\eta}+\frac{\delta\hat{H}^n}{\Delta\zeta}-\frac{\delta\hat{F}_v^n}{\Delta\xi}-\frac{\delta\hat{G}_v^n}{\Delta\eta}-\frac{\delta\hat{H}_v^n}{\Delta\zeta}-\hat{W}_{i,j}^n\right) \tag{8}$$

δ denotes central difference, I is the identity matrix 4x4 and $\hat{A}=\partial\hat{F}/\partial\hat{Q}$, $\hat{B}=\partial\hat{G}/\partial\hat{Q}$ and $\hat{C}=\partial\hat{H}/\partial\hat{Q}$ are the Jacobian matrices resulting from the linearization procedure. In general, eqn (8) is implemented in the following sequence:

$$\left(I+\frac{\Delta t}{2}\frac{\delta\hat{A}^n}{\Delta\xi}\right)\Delta\hat{Q}^{**}= \\ -\frac{\Delta t}{2}\left(\frac{\delta\hat{F}^n}{\Delta\xi}+\frac{\delta\hat{G}^n}{\Delta\eta}+\frac{\delta\hat{H}^n}{\Delta\zeta}-\frac{\delta\hat{F}_v^n}{\Delta\xi}-\frac{\delta\hat{G}_v^n}{\Delta\eta}-\frac{\delta\hat{H}_v^n}{\Delta\zeta}-\hat{W}_{i,j}^n\right) \quad 1^{st}\text{ step} \tag{9}$$

$$\left(I+\frac{\Delta t}{2}\frac{\delta\hat{B}^n}{\Delta\eta}\right)\Delta\hat{Q}^{*}=\Delta\hat{Q}^{**} \quad 2^{nd}\text{ step} \tag{10}$$

$$\left(I+\frac{\Delta t}{2}\frac{\delta\hat{C}^n}{\Delta\zeta}\right)\Delta\hat{Q}^{n+1}=\Delta\hat{Q}^{*} \quad 3^{rd}\text{ step} \tag{11}$$

$$\hat{Q}^{n+1}=\hat{Q}^n+\Delta\hat{Q}^{n+1} \quad 4^{th}\text{ step} \tag{12}$$

The values of the unknown variables at every point of the field are obtained by solving a block tri-diagonal system. The scheme is second-order accurate in space since central differences are used for the space derivatives.

To determine the position of free-surface, the depth-averaged continuity equation is coupled with the hydrodynamic equations and it is approximated by applying the same implicit scheme in 2D form, Klonidis and Soulis[7]. Since the new free-surface level position has been determined, the grid points, which are always located equidistantly along the vertical direction, are rearranged. The resulting curvilinear grid is transformed again into the local system before proceeding in the next iteration step. By this procedure, the model was highly unstable when trying to simulate problems with discontinuities at the free-surface, like shocks. After a lot of numerical experimentation it was found out that significant dispersion errors due to grid rearrangement are propagated.

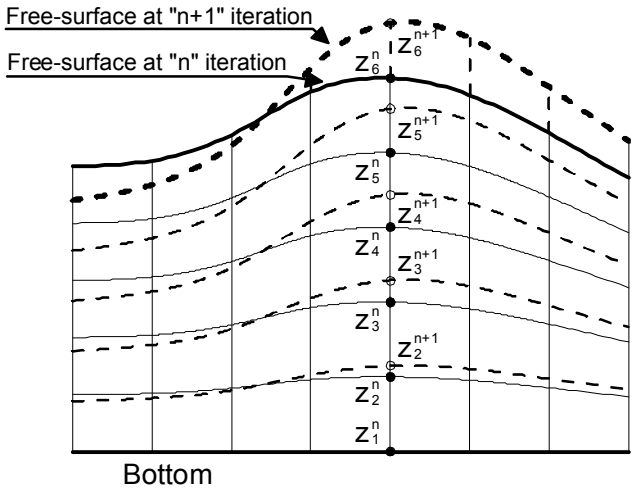

Figure 1. Vertical section of a hypothetical flow region with free-surface location between two adjacent iterations. Filled dots refer to the "n" iteration while empty dots refer to the "n+1" iteration

Indeed, from eqn (12) it is clear that since the free-surface has changed, the $\hat{Q}^{n}$ values related to the previous iteration step were calculated in different z- coordinates than the $\hat{Q}^{n+1}$ values related to the current iteration step. Figure 1 depicts a hypothetical flow region with six grid points along a single grid line. The grid points are rearranged due to the change of the free-surface level. To overcome this problem a simple but effective procedure is followed: Instead of using a single iteration step, two nested ones are used. Let's denote with *"n"* the basic or outer iteration step and with *"k"* the inner one. When the outer iteration starts all *Q (P,u,v,w,h)* values are initialized. The whole computational procedure, described by eqs (12)-(15), takes place within the inner iteration step but as long as the *"k"* iterations last every *Q* value is calculated as,

$$Q^{k+1} = Q^{n} + \Delta\hat{Q}^{k+1} \;,\; Q^{k+2} = Q^{n} + \Delta\hat{Q}^{k+2} \;, \ldots ,\; Q^{k+i} = Q^{n} + \Delta\hat{Q}^{k+i} \tag{13}$$

superscript $k+i$ stands for the k^{th} iteration step. The value Q^{n} which is referred to the outer iteration is kept constant during the inner iterations. It should be noted that the grid is rearranged within the inner iterations. The inner iterations continue until the convergence criterion related to the average percentage velocity is satisfied. Next, the outer iteration step changes to the next one and the *Q* values are updated as follows,

$$Q^{n+1} = Q^{k+i} \;,\; Q^{n+2} = Q^{k+i} \;, \ldots , Q^{n+j} = Q^{k+i} \tag{14}$$

superscript $n+j$ stands for the n^{th} iteration step. The outer iterations and consequently the whole computational procedure stops when two convergence criteria associated with the average percentage flow depth and the average percentage pressure are satisfied. Generally, the model starts with less than 15 inner iterations, which are decreased rapidly. As much as the outer convergence criterion is satisfied one or maximum two inner iterations are executed.

2.3 Boundary conditions

The law of the wall is used for the solid boundaries. According to this law the value of the velocity component normal to the solid boundary is set equal to zero. In addition, the values of $\Delta\hat{Q}^{**}$ along the upper and lower solid boundaries as well as at the bottom are determined by extrapolation from the adjacent interior grid nodes. On the free-surface the pressure *P* is equal to zero. For supercritical case flows the velocities v_x, v_y, v_z, the water depth *h* and the pressure *P* are specified at the inlet while at the outlet these variables are free to change and their values are extrapolated from the adjacent interior grid nodes. For subcritical case flow the velocities v_x, v_y, v_z are specified at the inlet, while the pressure *P* is extrapolated from the adjacent interior nodes. At the outlet the pressure *P* is fixed while the v_x, v_y, v_z velocities are extrapolated from the adjacent interior grid points.

3 SUPERCRITICAL FLOW IN CONVERGING CHANNEL

In this section a steady, highly supercritical flow in converging channel is tested. This type of flow was created in a straight wall contraction channel by Coles and Shintaku[8]. Among many CFD modelers, Liang et al.[9] simulated the same problem using an explicit, two-dimensional finite-volume model based on the solution of the Bhatnagar–Gross–Krook (BGK) Boltzmann equation. The current model computed results are compared with the available measurements as well as with the aforementioned BGK numerical scheme results. The channel consisted of two straight rectangular sections joined by a 1.50 m long straight-walled contraction. The contraction side-walls angle was 6.0°. The inlet width was 0.629 m and the outlet one was 0.314 m, while the bottom slopes were set equal to 0.0 $^{0}/_{00}$. The channel geometry is illustrated in figure 2.

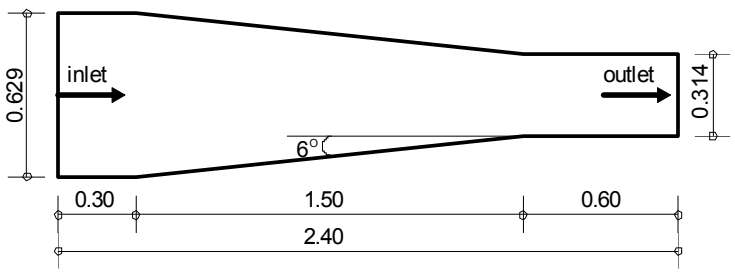

Figure 2. Converging channel geometry for supercritical flow type problem, Coles and Shintaku[4]. All dimensions in m.

The flow conditions included a steady flow discharge Q = 0.0451 m^3/s at a constant upstream flow depth h_0 = 0.0314 m which corresponds to an inlet Froude number of 4.0. Coles and Shintaku[8] did not report Chezy's roughness coefficient for the channel contraction. However, Molls and Chaudhry[10] after numerical experimentation found an optimum value of 84.1 $m^{1/2}/s$. To demonstrate the model's versatility in various grid resolutions, results obtained in two different hexahedral structured grids: a coarse consisting of 49610 nodes and a fine consisting of 98010 nodes. Inlet and outlet boundary conditions with respect to supercritical case flow were imposed while after numerical experimentation the optimum pseudo-compressibility factor β value was determined equal to 1.0. Figures 3 and 4 show a very good agreement between experimental data and current model results.

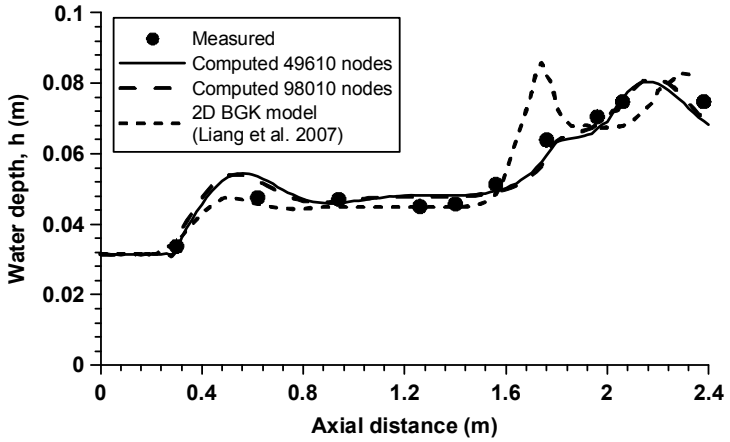

Figure 3. Sidewall water depth (m) comparison between current model predictions using 49610 nodes and 98010 nodes, 2D BGK model predictions, Liang et al.[12] and measurements for the converging channel after Coles and Shintaku[4]

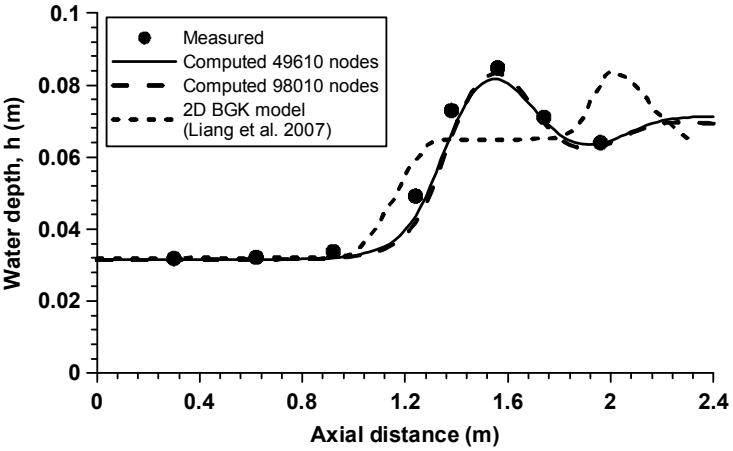

Figure 4. Centerline water depth (m) comparison between current model predictions using 49610 nodes and 98010 nodes, 2D BGK model predictions, Liang et al.[12] and measurements for the converging channel, Coles and Shintaku[4]

A strong shock wave is presented particularly along the centerline of the flume where its peak appears about 0.2 m upstream the end of contraction. By contrast, along the side walls the shock wave peak appears about 0.4 m downstream the end of contraction. It is also evident the superiority of the current 3D model compared to 2D BGK one regarding the accuracy in capturing the location of the shock waves. Finally, both coarse and fine grid

computed results are almost identical, demonstrating thus the ability of the model to give reliable results without the need of using very fine grids. The latter is very interesting considering the computational time saving aspect. Figures 5 and 6 show a comparison between measured and computed iso-depth (m) contours.

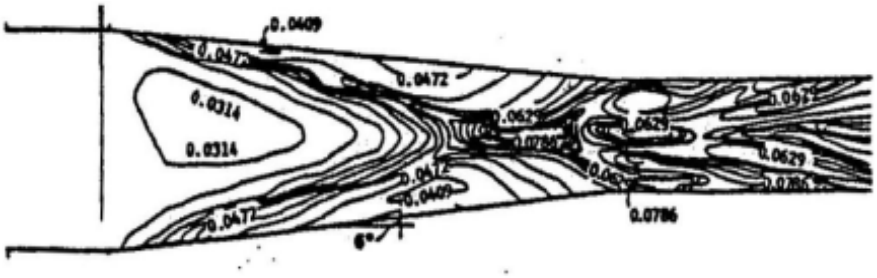

Figure 5. Measured iso-depth contours (m) for the converging channel, Coles and Shintaku[4]

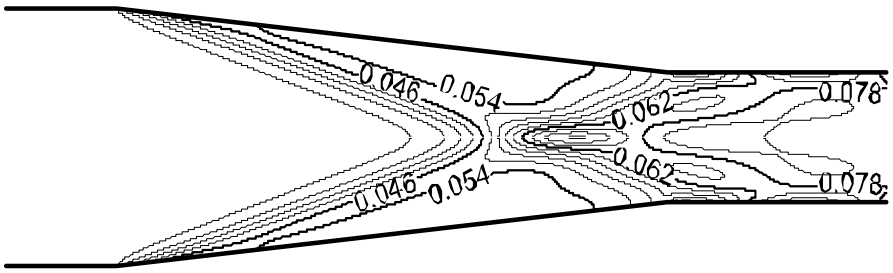

Figure 6. Computed iso-depth contours (m) for the converging channel, Coles and Shintaku[4]

As shown in the above figures perceptible oblique waves are developed reflecting on the centerline of the flume. Again, experimental data and computed results are in good agreement between each other.

4 CONCLUSIONS

In the present study the development and application of an implicit finite-volume numerical scheme capable of simulating three-dimensional, steady, free-surface flows in irregular geometry channels was presented. It is an alternative technique for the simulation of such flows where the free surface is treated as a moving boundary. The Navier-Stokes mass continuity equation was modified by utilizing the pseudo-compressibility technique initially introduced by Chorin[4]. The resulting equations system was transformed in a non-orthogonal, body fitted local coordinate system and solved using a second order implicit scheme resulted from the linearization of the governing equations. Furthermore, the use of the two-dimensional depth-averaged mass continuity equation as a simplified aspect of determining the free-surface location was proved to be adequate enough for the simulation of various problems where abrupt changes in the free-surface occur. To deal with significant numerical instabilities resulting from dispersion errors appearing during the abrupt change of the free-surface position, the use of two nested iteration steps as a new idea was presented analytically. All calculations take place within the inner step while the outer step updates the calculated variables preparing thus for the next inner iteration step. The value of turbulent kinematic viscosity was determined empirically with respect to bottom friction velocity, assuming a linear distribution of bottom shear stress over the depth. The model was fast in achieving convergence and it was applied to steady supercritical flow with the presence of shocks. Computed results were successfully compared with measurements while the model results surpassed the 2D numerical methods results. Also, the model performed remarkably well either in coarse or in fine grids allowing for computational time saving.

REFERENCES

[1] Pender, G. and Manson, J. R. (1994). "Developments in three dimensional numerical modeling of river flows". *Proc. 2nd Int. Conference on River Flood Hydraulics*, York, England.

[2] Ouillon, S. and Dartus, D. (1997). "Three-dimensional computation of flow around groyne". *Journal of Hydraulic Engineering, ASCE* 123(11), pp. 962-970.

[3] Feurich, R. and Olsen, R. B. (2012). "Finding free surface of supercritical flows-numerical investigation". *Engineering Applications of Computational Fluid Mechanics* 6(2), pp. 307-315.

[4] Chorin, A. J. (1967). "A Numerical Method for Solving Incompressible Viscous Flow Problems". *Journal of Computational Physics* 2(12).

[5] Liu, Z. (2001). *"Sediment transport"*. Laboratoriet for Hydraulik og Havnebygning Instituttet for Vand, Jord og Miljoteknik Aalborg Universitet, Finland.

[6] Klonidis, A. J. (2012). *"Computations and measurements of steady, three-dimensional flow with sediment transport around hydraulic structures"*. PhD Thesis, Democritus University of Thrace, Department of Civil Engineering, Xanthi, Greece.

[7] Klonidis, A. J. and Soulis, J. V. (2001). "An implicit scheme for steady two- dimensional free-surface flow calculation". *Journal of Hydraulic Research*, 39(3), pp. 1-10.

[8] Coles, D. and Shintaku, T. (1943). *"Experimental Relation Between Sudden Wall Angle Changes and Standing Waves in Supercritical Flow"*. B. S. Thesis, Lehigh University, Bethlehem, Pa.

[9] Liang, J. H., Ghidaoui, M. S., Deng, J. Q. and Gray, W. G. (2007). "A Boltzmann-based finite volume algorithm for surface water flows on cells of arbitrary shapes". *Journal of Hydraulic Research* 45(2), pp. 147-164.

[10] Molls, T. and Chaudhry, M. H. (1995). "Depth-averaged open-channel flow model". *Journal of Hydraulic Engineering, ASCE* 121(6), pp. 453-465.